Liquid metal embrittlement of a dual-phase Al0.7CoCrFeNi high-entropy alloy exposed to oxygen-saturated lead-bismuth eutectic

As Published: 10.1016/J.SCRIPTAMAT.2020.113652

Publisher: Elsevier BV

Persistent URL: https://hdl.handle.net/1721.1/136171

Version: Original manuscript: author's manuscript prior to formal peer review

Liquid metal embrittlement of a dual-phase $Al_{0.7}CoCrFeNi$ high-entropy alloy exposed to oxygen-saturated lead-bismuth eutectic

Xing Gong [a,*], Congying Xiang [b], Jiajun Chen [a], Xiaocong Liang [b], Zhiyang Yu [b,*], Thierry Auger [c], Michael P Short [d], Min Song [e], Yuan Yin [a,*]

[a] *Advanced Nuclear Energy Research Team, College of Physics and Optoelectronic Engineering, Shenzhen University, Shenzhen, 518060, China*
[b] *State Key Laboratory of Photocatalysis on Energy and Environment, College of Chemistry, Fuzhou University, Fuzhou, 350002, China*
[c] *PIMM, Arts et Metiers ParisTech, CNRS, Cnam, HESAM Université, 151 Blvd. de L'Hôpital 75013 Paris, France*
[d] *Department of Nuclear Science and Engineering, Massachusetts Institute of Technology (MIT), Cambridge, MA, 02139, USA*
[e] *State Key Laboratory of Powder Metallurgy, Central South University, Changsha, 410083, China*

*Corresponding authors
Email addresses: gongxing@szu.edu.cn (X. Gong); yuzyemlab@gmail.com (Z.Y. Yu); yinyuan@szu.edu.cn (Y. Yin)

Abstract

This paper reports a new liquid metal embrittlement (LME) system in which a dual-phase $Al_{0.7}CoCrFeNi$ (equimolar fraction) high-entropy alloy (HEA) is embrittled by lead-bismuth eutectic (LBE) at 350 and 500 °C. At 350 °C, (Ni, Al)-rich BCC phase is embrittled, leading to intragrain cracking within this phase, while the predominant cracking mode changes to BCC/FCC phase boundary decohesion at 500 °C. At both temperatures, cracks are rarely seen in the (Co, Cr, Fe)-rich FCC phase, indicating that this phase is immune to LME. Furthermore, the results suggest a transition from an adsorption-dominated LME mechanism at 350 °C to a phase boundary wetting-dominated LME mechanism at 500 °C.

Keywords: LBE; Liquid metal embrittlement; High-entropy alloys; Cracking; Phase boundary wetting

Liquid lead-bismuth eutectic ($Pb_{44.5}Bi_{55.5}$, wt%, LBE) is an important working fluid for Gen IV fast reactors and accelerator driven transmutation systems (ADS), due to its beneficial thermohydraulic and neutronic properties as well as inherent safety [1]. Nevertheless, the deployment of this technology is technically impeded by incompatibility issues of steels when exposed to LBE, including the so-called liquid metal embrittlement (LME) and liquid metal corrosion (LMC) [1, 2]. LME occurs mainly in ferritic/martensitic steels (F/M, e.g., T91, HT9, and EP823) at around 350°C, leading to severe deterioration of ductility and toughness of these steels when stressed in LBE [3-8]. LMC can occur in the F/M steels and austenitic stainless steels (AuSS, e.g., 316L and 15-15Ti), manifested by either surface oxidation when LBE is rich in oxygen or by selective leaching of the steel elements (e.g., Ni, Mn, Cr, and Fe) when oxygen in LBE is poor [9]. In particular, the locally-enhanced dissolution, also called "pitting", represents the most undesired corrosion mode and poses a serious threat to thin-walled components, such as fuel cladding and heat exchanger tubes [10-15]. These issues can jeopardize the safe operation of the reactors.

To better take the advantage of LBE-cooled fast reactors, it is necessary to explore new materials with higher resistance to the harsh LBE environment at elevated temperatures. In recent years, high-entropy alloys (HEAs) have been receiving increased research interests for their unique microstructures and appealing properties

[16-18]. Unlike traditional alloys that contain only a couple of major elements, HEAs consist of at least five principal elements, leading to a series of interesting characteristics, such as high entropy of the whole alloy system, sluggish diffusion, and strong lattice distortion, etc. A large number of studies have demonstrated that HEAs possess excellent mechanical properties [16-18], high corrosion and stress corrosion cracking resistance [19-21], as well as good irradiation resistance [22, 23]. Among them, the $Al_xCoCrFeNi$ type is one of the most investigated HEAs [16, 24].

In this paper, an $Al_{0.7}CoCrFeNi$ (at.%) HEA was selected for the LME study, considering that this alloy is a dual-phase structure (FCC + BCC) and hence has a good balance of strength and ductility [24]. In addition, this alloy contains 14.89 at.% (i.e., about 7.73 wt.%) Al and thus can form a passivating and protective alumina scale that is very important for corrosion resistance [25]. The phase diagrams with lead or bismuth of most of the constituents of the alloy (Al, Fe, Cr, Co) show an immiscibility gap in the solid state with limited high temperature solubility [26]. Only the Ni/Bi system shows some intermetallic compounds. In most cases, the immiscibility between the solid and the liquid phase is a good indicator for a possible LME behavior. Therefore, a few screening tensile tests were performed to assess the LME susceptibility of this alloy in contact with LBE at 350 and 500 °C. The results show that this alloy is susceptible to LME, manifested by a significant reduction in total elongation to rupture. To the best of our knowledge, this is a new LME system that was not reported in the past. The underlying LME mechanism of this system is discussed, based on multiscale microstructural characterizations.

The $Al_{0.7}CoCrFeNi$ alloy was fabricated by vacuum induction melting at 1700°C. The obtained cast ingots were then manufactured into cylindrical tensile specimens with a gauge length of 15 mm and a gauge diameter of 3 mm. The specimens were tested in oxygen-saturated LBE at 350 and 500 °C using our test facility "LABET-1" [27]. Before starting the tests, the specimens were pre-exposed to LBE at 500 °C for about 20 h. Reference tests were performed in air at the same temperatures. All tests were carried out under a nominal strain rate of 5×10^{-5} s^{-1}.

The original microstructure of the $Al_{0.7}CoCrFeNi$ alloy was examined by scanning electron microscope (SEM, Thermofisher Scientific Scios), X-ray diffraction (XRD, Miniflex600), electron backscatter diffraction (EBSD, Oxford, NordlysMax), and transmission electron microscopy (TEM, Thermofisher Scientific Talos F200s). After the tensile testing in LBE, the fractured specimen was cleaned in a chemical solution composed of CH_3COOH (acetic acid), CH_3CH_2OH (ethanol) and H_2O_2 (hydrogen peroxide) with a volume ratio of 1:1:1 for SEM fractographic examinations. Focused-ion beam (FIB, Thermofisher Scientific Helios600i) was used to prepare site-specific lamellas at crack tips for TEM examinations.

SEM micrograph and XRD pattern in **Figs. 1a** and **1b** show that the $Al_{0.7}CoCrFeNi$ alloy is composed of an FCC phase and a BCC phase. The two phases are regularly spaced by each other and have lamellae-like morphology. The larger phase has an FCC structure, while the smaller phase is recognized as a BCC structure (**Fig. 1c)**. High-angle annular dark field (HAADF) image and EDS maps in **Figs. 1d** and **1e** reveal that the FCC phase is rich in Co, Cr and Fe with a thickness of 1~5 μm, while Al and Ni are

the major constitutive elements of the BCC phase and this phase mostly has a thickness ranging from several hundred nanometers to 1μm. These results are in good agreement with those reported by Wang et al. [24].

Fig. 2 presents the engineering tensile stress-strain curves of the $Al_{0.7}CoCrFeNi$ alloy tested in oxygen-saturated LBE and air at 350 and 500 °C. It can be seen that this alloy shows high strength and acceptable ductility when tested in air at both temperatures (see the dashed lines). When tested in LBE, strength is not altered, but strong ductility loss occurs in comparison to that in air. This is a typical sign of LME. The ductility loss is more severe at 350°C (by ~70%) than that at 500°C (by ~50%).

Fig. 3 examines the fracture surfaces and longitudinal cross-sections of the specimens tested in air and LBE at 350 and 500°C, showing large differences. For the specimen tested in air at 350°C (**Fig. 3a**), the fracture surface shows a mixture of cleavage of the (Ni, Al)-rich BCC phase and tearing of the (Co, Cr, Fe)-rich FCC phase. This implies that the (Ni, Al)-rich BCC phase is already brittle at 350 °C, while the (Co, Cr, Fe)-rich FCC phase may have some ductility. This is to be expected, since nickel aluminides intermetallics are known to be brittle at low temperatures [28]. For the specimen tested at the same temperature but in LBE (**Fig. 3b**), the fracture surface does not show evident differences in comparison to that in air (**Fig. 3a**), but fiber-like structures start to show up. The SEM backscatter micrograph of the longitudinal cross-section reveals more clearly the cracking paths (**Fig. 3c**). It can be seen from this figure that the cracks are filled completely with LBE up to the crack tips, suggesting good wetting of LBE on the crack walls. The cracks propagate mainly inside the (Ni, Al)-

rich BCC phase, with only a small part going along the BCC/FCC phase boundaries. Combining this observation with the ductility loss shown in **Fig. 2**, it can be concluded that the (Ni, Al)-rich BCC phase is susceptible to LME. One may notice that the (Co, Cr, Fe)-rich FCC phase can arrest the crack tips (see the arrows in **Fig. 3c**). This observation indicates that the FCC phase is not susceptible to LME. The LME insensitivity of this phase is similar to that of another FCC-structured HEA ($Fe_{40}Mn_{10}Ni_{10}Co_{20}Cr_{20}$, at.%) reported in our previous work [27]. Increasing the testing temperature from 350 to 500 °C improves the ductility of the alloy in air, since cleavage of the BCC phase is not as evident as that at 350 °C and ductile dimpling is visible locally (**Fig. 3d**). The fracture surface of the specimen tested in LBE at 500 °C is much different from that tested in air at the same temperature (**Fig. 3e)**. It can be seen that massive fiber-like structures are visible on the fracture surface. The formation of these fiber-like structures is a result of decohesion of BCC/FCC phase boundaries, as shown in **Fig. 3f**. It is clearly seen from this figure that the quantity of the locations where LBE penetrates into the BCC/FCC phase boundaries as a thin intergranular film is remarkably increased (see the arrows and dashed circle) compared to that at 350 °C (**Fig. 3c**), though a few cracks propagating inside the BCC phase are still visible. These results suggest that the LME mechanism of this alloy at 500 °C is most likely linked to phase boundary wetting with an intergranular penetration of LBE (with eventually a diffusive step).

The HAADF image in **Fig. 4a** shows that a crack in the specimen tested in LBE at 350 °C propagates inside the BCC phase that in fact is a single grain. The high-

resolution TEM (HRTEM) images in **Figs. 4b** and **4c** reveal that the cracking planes change alternately from the main plane $(\bar{2}11)$ to the secondary plane (200), and finally this crack is arrested by the $(02\bar{2})$ and (064) planes of the FCC phase. Increasing the testing temperature to 500°C leads to mainly the decohesion of the BCC/FCC phase boundaries and a small amount of BCC phase cracking (**Fig. 5a**). At this relatively high temperature, the main cracking plane in the BCC phase falls into the same crystallographic plane family as that at 350°C, i.e., $(2\bar{1}1)$, while the secondary cracking plane changes to $(0\bar{1}1)$, as shown in **Fig. 5b**. In the case of the phase boundary decohesion (**Figs. 5c and 5d**), LBE penetrates preferentially into the $(2\bar{1}1)_{bcc}//(11\bar{1})_{fcc}$ and $(01\bar{1})_{bcc}//(200)_{fcc}$ phase boundaries (the main cracking planes mate while the secondary planes mate), forming a very thin LBE film with a thickness of about 30 nm (**Fig. 5c**). Both specimens tested at 350 and 500 °C do not show formation of new phases along the cracking paths or at the crack tips.

LME systems can be categorized into two groups. One group is grain boundary wetting, in which the grain boundary energy (γ_{gb}) that drives liquid metal into grain boundaries of solid metal is overwhelming over the interfacial energy of the solid metal/liquid metal contacting interface (γ_{sl}) that rejects liquid metal from the grain boundaries of solid metal. In this case, liquid metal can spontaneously enter the grain boundaries of the solid metal. Those systems, including Al/Ga [29], Cu/Bi [30, 31], Ni/Bi [32, 33], Mo/Ni[34], etc., are typical cases of this group. The other group needs external factors, such as stress, temperature, etc., to aid the liquid metal to attack the grain boundaries or bulk of the solid metal, such as the T91/LBE and FeCrAl/LBE

systems [35, 36]. At 350 °C, the mechanism of the LME system in this study is most likely governed by adsorption of LBE at the crack tip and weakening of the atomic bonds of the alloy [37, 38], since the cracks propagate mainly inside the BCC phase while LBE penetration into grain or phase boundaries is rarely seen. Note that the BCC phase is already very brittle at 350 °C as expected (**Fig. 3a**). This means that LBE makes this phase even more brittle due to the remarkable ductility loss (**Fig. 2**). When the temperature increases to 500 °C, the ductility of the BCC phase improves (**Fig. 3d**). NiAl has a very high ductile-brittle transition temperature (DBTT, ~1000°C) [28], but the BCC phase may not be a pure NiAl phase (**Fig. 1e**) and the small amount of Co may have significantly lowered down its DBTT. This may partly account for the much less observed cracks inside the BCC phase at 500 °C than at 350 °C. The significantly increased number of the BCC/FCC phase boundary cracking at 500 °C (**Figs. 3e** and **3f**) indicates a phase boundary wetting transition of LBE is enhanced. Thus, this is a new LME system involving phase boundary wetting at the high temperature, in addition to the systems mentioned earlier. The LME cracking follows mostly the low index crystallographic planes (**Figs. 4** and **5**), which is in line with the lowest energy criterion. This phase boundary wetting mechanism is different from the steel/Zn system in which new intermetallic phases or phase transformation occurs at the penetration front [39]. In our case, new phases are not detected by HRTEM, but ordered segregation structures at atomic scale cannot be excluded as similar to what is observed in the Ni/Bi system [32, 33]. More importantly, the phase boundary wetting transition must be enhanced by the tensile stresses that can open the interatomic space in the vicinity of the liquid metal

penetration front, because the stress-free corrosion test result presented in **Fig. S1** shows a maximum LBE penetration depth of 257 μm was formed after exposure for 500 h, corresponding to a penetration rate of only 0.514 μm/h, while the LME-induced sudden stress drop in **Fig. 2** occurs in less than one second, corresponding to a cracking rate of as high as ~3000 μm/s (the specimen diameter is 3 mm and the sudden stress drop takes place prior to necking).

In summary, this paper reports a new LME system. It is found that the dual-phase (FCC + BCC) $Al_{0.7}CoCrFeNi$ (equimolar fraction) high-entropy alloy is embrittled by LBE at 350 and 500°C. The LME characteristics are temperature-dependent. At 350°C, cracks propagate mainly within the (Ni, Al)-rich BCC phase and along certain low-index planes, indicating that the BCC phase is susceptible to LME. At 500°C, cracking at the BCC/FCC phase boundaries is the dominant failure mode. This temperature dependence of the LME cracking behaviors suggests a transition from an adsorption-dominated LME mechanism at 350°C to a phase boundary wetting-controlled LME mechanism at 500°C. At both temperatures, cracks are rarely observed in the FCC phase, implying that this phase is immune to LME. This LME case with an intermetallic phase has some parallels with the case of beta-brass LME in the ordered B2 (CsCl type) composition range as well [40]. Given the strong LME susceptibility, this HEA material is not recommended for use in LBE environment.

Acknowledgements

This work is financially supported by Natural Science Foundation of China (Grant

No. 51701170 and 51801129) and Natural Science Foundation of Shenzhen University, China (Grant no. 85304-00000302).

References

[1] OECD/NEA, Handbook on lead-bismuth eutectic alloy and lead properties, materials compatibility, thermal-hydraulics and technologies, 2015.

[2] X. Gong, R. Li, M.Z. Sun, Q.S. Ren, T. Liu, M.P. Short, J Nucl. Mater. 482 (2016) 218-228.

[3] D. Gorse, T. Auger, J.-B. Vogt, I. Serre, A. Weisenburger, A. Gessi, P. Agostini, C. Fazio, A. Hojná, F. Di Gabriele, J Nucl. Mater. 415 (2011) 284-292.

[4] E. Stergar, S.G. Eremin, S. Gavrilov, M. Lambrecht, O. Makarov, V. Lakovlev, J Nucl. Mater. 473 (2016) 28-34.

[5] X. Gong, P. Marmy, Y. Yin, J Nucl. Mater. 509 (2018) 401-407.

[6] F. Ersoy, S. Gavrilov, K. Verbeken, J Nucl. Mater. 472 (2016) 171-177.

[7] A. Hojná, P. Halodová, M. Chocholoušek, Z Špirit, L. Rozumová, Corros. Rev. 38 (2020) 183-194.

[8] I. Proriol Serre, J.-B. Vogt, J. Nucl. Mater. 531 (2020) 152021.

[9] J.S. Zhang, N. Li, J Nucl. Mater. 373 (2008) 351-377.

[10] V. Tsisar, C. Schroer, O. Wedemeyer, A. Skrypnik, J. Konys, J Nucl. Mater. 454 (2014) 332-342.

[11] V. Tsisar, C. Schroer, O. Wedemeyer, A. Skrypnik, J. Konys, J Nucl. Mater. 468 (2016) 305-312.

[12] K. Lambrinou, E. Charalampopoulou, T. Van der Donck, R. Delville, D. Schryvers, J Nucl. Mater. 490 (2017) 9-27.

[13] K. Lambrinou, V. Koch, G. Coen, J. Van den Bosch, C. Schroer. J Nucl. Mater.

450 (2014) 244-255.

[14] V. Tsisar, C. Schroer, O. Wedemeyer, A. Skrypnik, J. Konys, J Nucl. Eng. Rad. Sci. 5 (2019) 031201.

[15] C. Schroer, V. Tsisar, A. Durand, O. Wedemeyer, A. Skrypnik, J. Konys, J Nucl. Eng. Rad. Sci. 5 (2019) 011006.

[16] E.P. George, W.A. Curtin, C.C. Tasan, Acta Mater. 188 (2020) 435-474.

[17] Z.Z. Li, S.T. Zhao, R.O. Ritchie, M.A. Meyers, Prog. in Mater. Sci. 102 (2019) 296-345.

[18] P. Sathiyamoorthi, H.S. Kim, Prog. in Mater. Sci. 2020, In press, https://doi.org/10.1016/j.pmatsci.2020.100709.

[19] Y.Z. Shi, L. Collins, R. Feng, C. Zhang, N. Balke, P.K. Liaw, B. Yang, Corros. Sci. 133 (2018) 120-131.

[20] H. Luo, W.J. Lu, X.F. Fang, D. Ponge, Z.M. Li, D. Raabe, Mater. Today, 21 (2018) 1003-1009.

[21] Y.K. Zhao, D.H. Lee, M.Y. Seok, J.A. Lee, M.P. Phaniraj, J.Y. Suh, H.Y. Ha, J.Y. Kim, U. Ramamurty, J. Jang, Scripta Mater. 135 (2017) 54-58.

[22] K. Jin, C.Lu, L.M. Wang, J. Qu, W.J. Weber, Y. Zhang, H. Bei, Scripta Mater. 119 (2016) 65-70.

[23] T.F. Yang, W. Guo, J.D. Poplawsky, D.Y. Li, L. Wang, Y. Li, W.Y. Hu, M.L. Crespillo, Z.F. Yan, Y. Zhang, Y.G. Wang, S.J. Zinkle, Acta Mater. 188 (2020) 1-15.

[24] W.R. Wang, W.L. Wang, S.C. Wang, Y.C. Tsai, C.H. Lai, J.W. Yeh, Intermetallics, 26 (2012) 44-51.

[25] J. Lu, Y. Chen, H. Zhang, L. Li, L.M. Fu, X.F. Zhao, F.W. Guo, P. Xiao, Corros. Sci. 170 (2020) 108691.

[26] Phase Equilibria, Crystallographic and Thermodynamic Data of Binary Alloys.

Landolt-Börnstein - Group IV Physical Chemistry. Vol. 5. Springer.

[27] X. Huang, X. Gong, M. Song, J.J. Chen, F.Y. Hu, Y. Yin, J. Xiao, H. Wang, H. Wang, H.R. Gong, Y.B. Deng, B. Pang, Y.C. Li, J Nucl. Mater. 528 (2020) 151859.

[28] A. Lasalmonie, Intermetallics, 14 (2006) 1123-1129.

[29] E. Pereiro-Lopez, W. Ludwig, D. Bellet, P. Cloetens, C. Lemaignan, Phys. Rev. Lett. 95 (2005) 215501.

[30] A. Kundu, K.M. Asl, J. Luo, M.P. Harmer, Scripta Mater. 68 (2013) 146-149.

[31] G. Duscher, M. F. Chisholm, U. Alber, M. Rühle, Nat. Mater. 3 (2004) 621-626.

[32] J. Luo, H. Cheng, K.M. Asl, C.J. Kiely, M.P. Harmer. Science, 333 (2011) 1730-1733.

[33] Z.Y. Yu, P.R. Cantwell, Q. Gao, D. Yin, Y.Y. Zhang, N.X. Zhou, G.S. Rohrer, M. Widom, J. Luo, M.P. Harmer, Science, 358 (2017) 97-101.

[34] X.M. Shi, J. Luo, Appl. Phys. Let. 94 (2009) 251908.

[35] X. Gong, P. Marmy, A. Volodin, B. Amin-Ahmadi, L. Qin, D. Schryvers, S. Gavrilov, E. Stergar, B. Verlinden, M. Wevers, Corros. Sci. 102 (2016) 137-152.

[36] X. Gong, J.J. Chen, F.Y. Hu, C.Y. Xiang, Z.Y. Yu, J. Xiao, H. Wang, H.R. Gong, H. Wang, C.H. Liu, Y.B. Deng, B. Pang, X. Huang, Y.C. Li, Y. Yin, Corros. Sci. 165 (2020) 108364.

[37] N.S. Stoloff, T.L. Johnston, Acta Metall. 11 (1963) 251-256.

[38] A.R.C. Westwood, M.H. Kamdar, Philos. Mag. 8 (1963) 787-804.

[39] L. Cho, H. Kang, C. Lee, B.C. De Cooman, Scripta Mater. 90 (2014) 25-28.

[40] M.M. Shea, N.S. Stoloff, Mater. Sci. Eng. 12 (1973) 245-253.

Figure captions

Fig. 1. SEM micrograph (a), XRD pattern (b), EBSD phase map (c), HAADF image (d) and EDS maps (e) of the as-received dual-phase $Al_{0.7}CoCrFeNi$ high-entropy alloy. Note: the BCC phase and FCC phase are identified by EBDS using standard BCC-structured NiAl and FCC-structured austenite PDF cards, respectively (c).

Fig. 2. Engineering tensile stress-strain curves of the dual-phase $Al_{0.7}CoCrFeNi$ high-entropy alloy tested in oxygen-saturated LBE and air at 350 and 500°C (the curves are not corrected with the compliance of the mechanical testing machines).

Fig. 3. SEM micrographs of the fracture surfaces (a,b,d,e) and longitudinal cross-sections (c, f) of the dual-phase $Al_{0.7}CoCrFeNi$ high-entropy alloy after testing in LBE and air at 350 and 500°C.

Fig. 4. A HAADF image (a) and two HRTEM images (b,c) showing that the crack propagates inside the BCC phase and along certain low index planes, and finally is arrested by the FCC phase. The TEM lamellae was extracted from a specimen tested in oxygen-saturated LBE at 350 °C.

Fig. 5. A HAADF image (a) and three HRTEM images (b,c,d) showing that cracks propagate either inside the BCC phase or along the BCC/FCC phase boundaries. The TEM lamellae was extracted from a specimen tested in oxygen-saturated LBE at 500 °C.

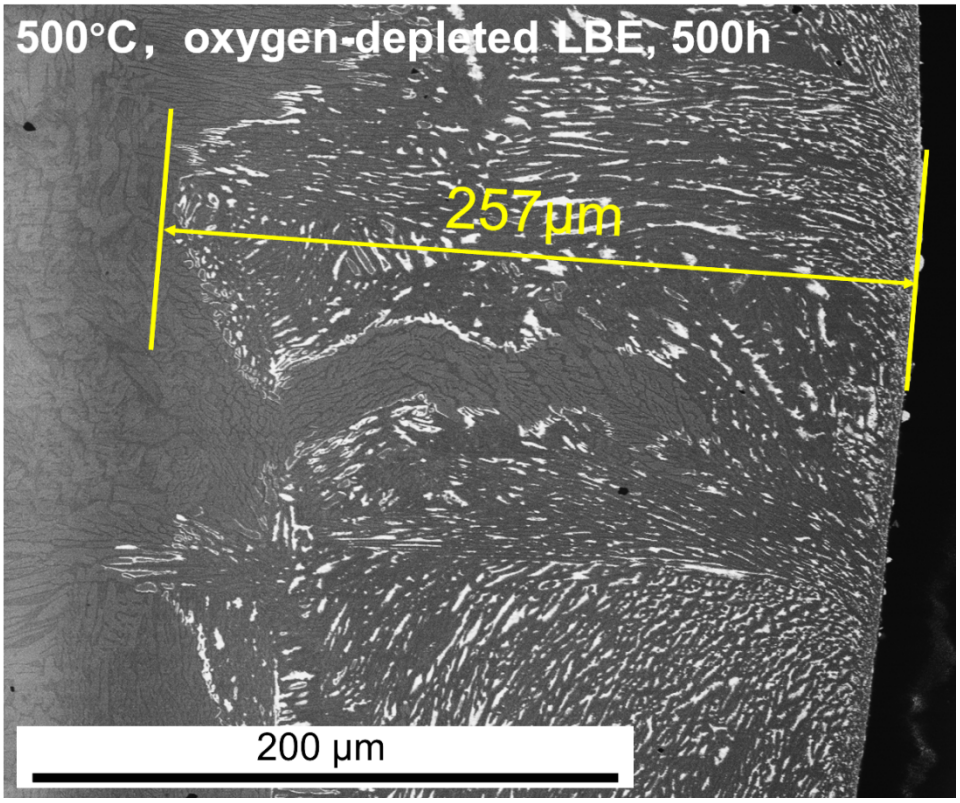

Fig. S1. SEM back-scatter micrograph showing that LBE penetrates along the BCC/FCC phase boundaries of $Al_{0.7}CoCrFeNi$ alloy exposed to oxygen-depleted LBE ($Co = 10^{-12} \sim 10^{-15}$wt%) at 500 °C for 500h, forming a maximum penetration depth of 257 μm. Thus, the corresponding penetration rate is about 0.514 μm/h under the stress-free condition.

Fig. 1

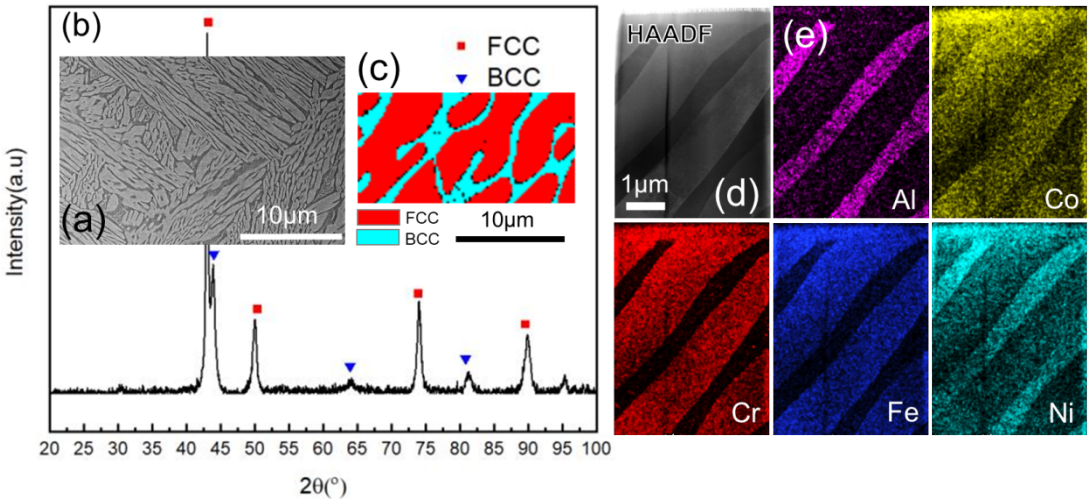

Fig. 2

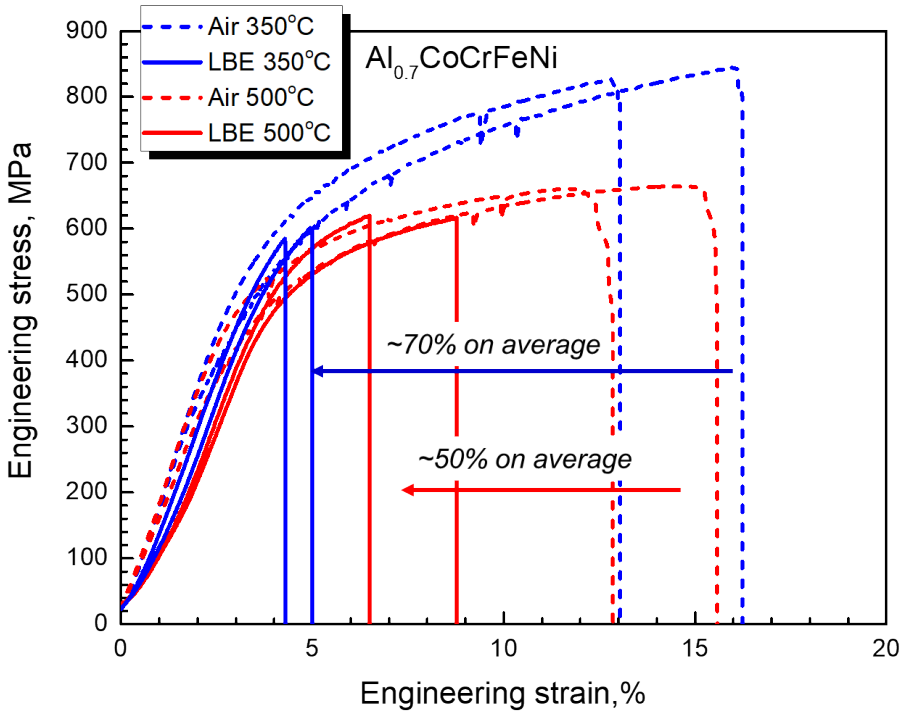

Fig. 3

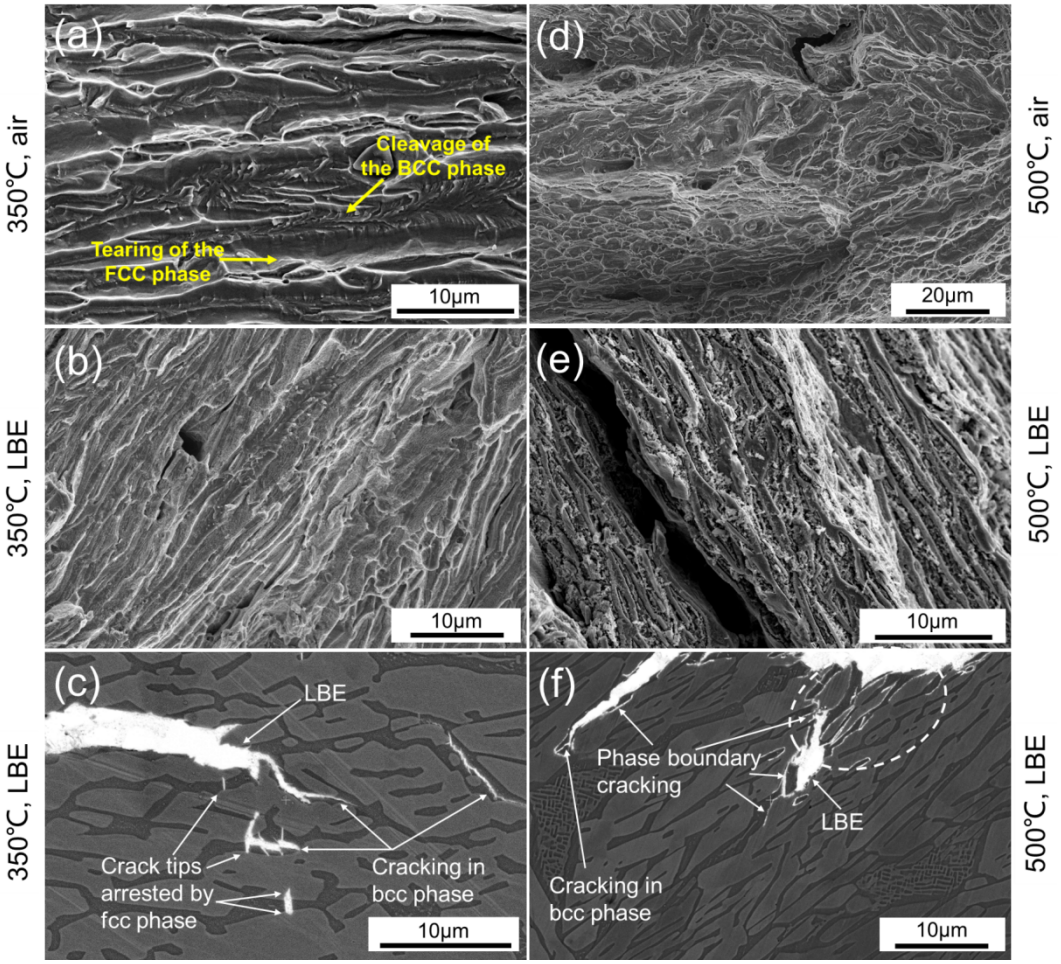

Fig. 4

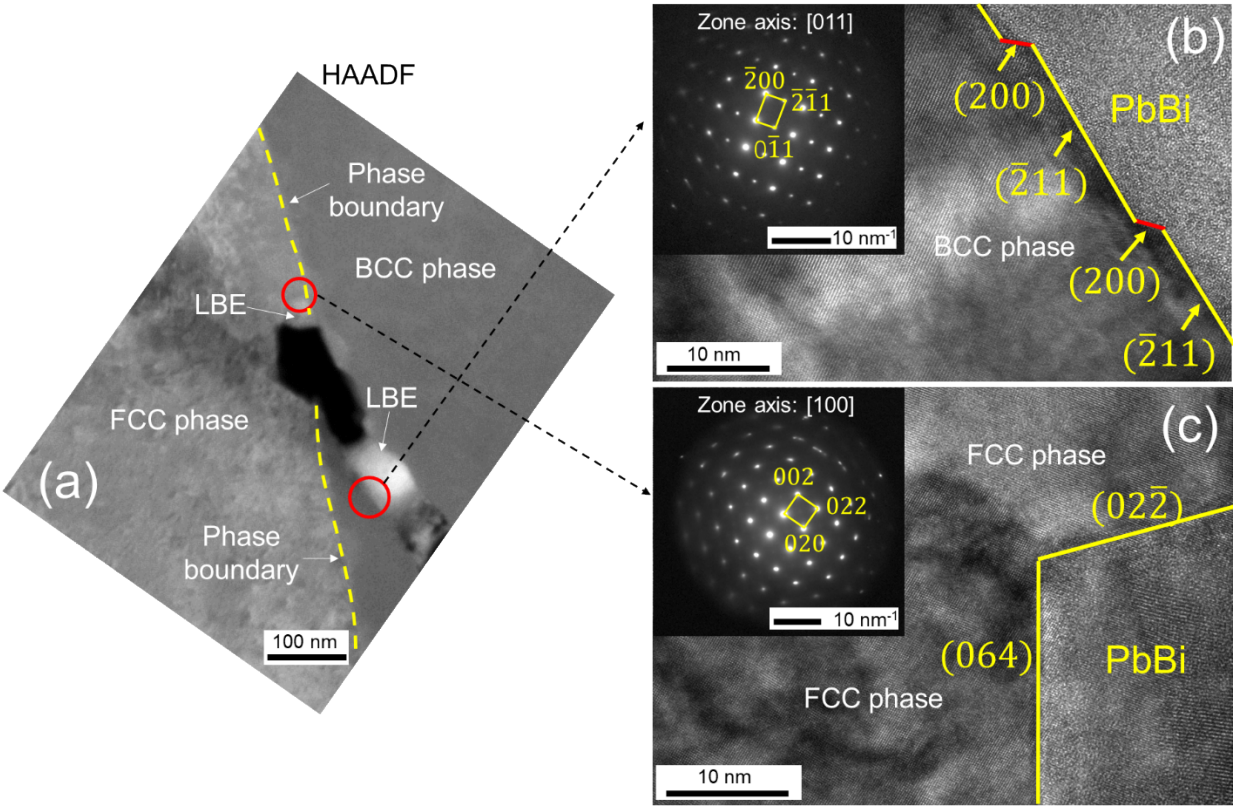

Fig. 5